High-speed AFM reveals subsecond dynamics of cardiac thin filaments upon Ca^{2+} activation and heavy meromyosin binding

Oleg S. Matusovsky[a], Alf Mansson[b], Malin Persson[a,b], Yu-Shu Cheng[a], and Dilson E. Rassier[a,1]

[a]Department of Kinesiology and Physical Education, McGill University, Montreal, QC H2W 1S4, Canada; and [b]Department of Chemistry and Biomedical Sciences, Linnaeus University, SE-391 82 Kalmar, Sweden

Edited by Roger Craig, University of Massachusetts Medical School, Worcester, MA, and accepted by Editorial Board Member Yale E. Goldman July 1, 2019 (received for review February 26, 2019)

High-speed atomic force microscopy (HS-AFM) can be used to study dynamic processes with real-time imaging of molecules within 1- to 5-nm spatial resolution. In the current study, we evaluated the 3-state model of activation of cardiac thin filaments (cTFs) isolated as a complex and deposited on a mica-supported lipid bilayer. We studied this complex for dynamic conformational changes 1) at low and high [Ca^{2+}] (pCa 9.0 and 4.5), and 2) upon myosin binding to the cTF in the nucleotide-free state or in the presence of ATP. HS-AFM was used to directly visualize the tropomyosin–troponin complex and Ca^{2+}-induced tropomyosin movements accompanied by structural transitions of actin monomers within cTFs. Our data show that cTFs at relaxing or activating conditions are not ultimately in a blocked or activated state, respectively, but rather the combination of states with a prevalence that is dependent on the [Ca^{2+}] and the presence of weakly or strongly bound myosin. The weakly and strongly bound myosin induce similar changes in the structure of cTFs as confirmed by the local dynamical displacement of individual tropomyosin strands in the center of a regulatory unit of cTF at the relaxed and activation conditions. The displacement of tropomyosin at the relaxed conditions had never been visualized directly and explains the ability of myosin binding to TF at the relaxed conditions. Based on the ratios of nonactivated and activated segments within cTFs, we proposed a mechanism of tropomyosin switching from different states that includes both weakly and strongly bound myosin.

thin filaments | muscle contraction | HS-AFM

Muscle contraction is the result of actin–myosin interactions that are regulated by Ca^{2+} through the regulatory proteins troponin (Tn) and tropomyosin (Tm) located on the actin filaments. The complex of actin, Tn, and Tm form highly structured thin filaments (TFs). The neighboring ∼40-nm-long α-helical Tm molecules are assembled by head-to-tail interactions to produce a long cable along the TF. Each of the Tm molecules contact with 7 actin monomers and the Tn-T subunit of the Tn complex (1–3). The 2 other subunits of Tn, Tn-I and Tn-C, interact with actin and bind Ca^{2+}, respectively. Upon Ca^{2+} binding to Tn-C, conformational rearrangements are triggered in the Tm–Tn complex resulting in azimuthal displacement of Tm away from the myosin binding site on actin (4–6).

The steric blocking model originally proposed the correlation between Tm displacement and existence of inactivated ("OFF") and activated ("ON") states of the TFs (7, 8). According to this model, at low Ca^{2+} concentration the location of Tm blocks myosin binding sites, whereas at high Ca^{2+} concentration Tm moves azimuthally around actin to expose these sites (9, 10). Based on new structural and biochemical data, the model gained complexity, with the proposal of 3 TF structural states: blocked (B), closed (C), and myosin or open (M), which correspond to relaxing, activating, and myosin-bound conditions (11). According to the 3-state model, in the absence of Ca^{2+} the Tn complex is tightly bound to Tm (through Tn-T subunits) and actin (through Tn-I subunits) and able to hold the Tm in a B-state, where Tm protects actin from binding to myosin heads (12). When Ca^{2+} is bound to the Tn-C subunit, binding between the Tn subunits becomes weaker (13) and releases Tm from actin. This allows Tm to move around the axis of the actin filament to a C-state, where actin becomes available for weak binding of myosin heads. With the transition from weak to strong actin–myosin binding, the myosin heads transfer Tm to an open state, or M-state, making several neighboring myosin binding sites on actin available for myosin binding (11, 14, 15).

The 3-state and modified steric blocking models rely on biochemical and X-ray data (7, 8, 16–19) as well as on structural analysis by electron microscopy (EM) or cryo-EM. This both involves analysis of negatively stained and frozen F-actin–Tm complexes at low and high Ca^{2+} concentrations (2, 9, 10, 20–25). Although the direct visualization of these structures at the near-atomic level greatly benefits our understanding of the functional mechanisms of TF activation, the EM and cryo-EM structures were studied under a defined set of conditions, representing static averaged "snapshots" of the F-actin–Tm–Tn complex, where Tm is in a fixed position on the actin surface. During reconstruction and averaging of the data, the variations of the Tm–actin interaction in the presence of Ca^{2+} and myosin

Significance

The advent of high-speed atomic force microscopy (HS-AFM) changed the field of biology considerably. HS-AFM is the only method where in situ dynamics of biological samples and imaging can be coupled with a spatial resolution of 1 to 5 nm in the horizontal direction. Unlike electron or cryo-electron microscopy, HS-AFM does not require fixation or freezing of the samples, and has the ability to derive kinetic parameters by recording the live movements of single-molecule dynamics. In this paper, we used HS-AFM to investigate directly the mechanisms of cardiac muscle activation. We visualized the muscle regulatory tropomyosin–troponin complex movements during activation by calcium or myosin (motor that drives contraction), and the structural transitions that happen during these events.

Author contributions: O.S.M. and D.E.R. designed research; O.S.M., M.P., and Y.-S.C. performed research; D.E.R. contributed new reagents/analytic tools; O.S.M., A.M., M.P., and D.E.R. analyzed data; and O.S.M., A.M., and D.E.R. wrote the paper.

The authors declare no conflict of interest.

This article is a PNAS Direct Submission. R.C. is a guest editor invited by the Editorial Board.

[1]To whom correspondence may be addressed. Email: dilson.rassier@mcgill.ca.

This article contains supporting information online at www.pnas.org/lookup/suppl/doi:10.1073/pnas.1903228116/-/DCSupplemental.

Published online July 29, 2019.

can be lost, which represents a challenge for identification of Tm shifts after 3D helical reconstruction (14, 26).

It has been shown that Tm might be localized in different positions on the actin surface even under relaxing conditions (8, 27), but this has not been visualized directly. Furthermore, it is still unclear how such different positions could be implicated in a cooperativity of TF activation in the presence of Ca^{2+}, and the weakly or strongly bound myosin. Finally, the canonical mechanism of TF activation by Ca^{2+} and strong myosin binding predicted in the previous studies have never been observed in a dynamic situation with real-time motions at the nanometer resolution. Here, we aimed to fill this gap by using high-speed atomic force microscopy (HS-AFM), which allows the direct 3D visualization of conformational changes and thermal motions of native cardiac TFs (cTFs) and cTF–myosin complexes in physiological solutions, under either relaxing or activating conditions. Importantly, these measurements were made without sample processing and fixation. The HS-AFM movies thus demonstrated the Ca^{2+}-induced Tm movement accompanied by the transition of the actin crossover peak heights as an index of changed structure of cTFs under dynamic conditions. These results advance our understanding of cTF activation that will benefit investigation of structural changes in the Tm–Tn complex caused by various cardiac myopathies.

Results

Ca^{2+} Sensitivity of Cardiac Thin Filaments. Before performing HS-AFM experiments, we assessed the Ca^{2+} sensitivity of the native cTFs (including actin, Tm, and Tn complexes). The Mg^{2+}-ATPase of myosin in the presence of cTFs was significantly increased in the presence of Ca^{2+} in a concentration-dependent manner ($P = 0.011$; *SI Appendix*, Fig. S1*C*). In addition, the myosin-driven velocity of cTFs and the fraction of moving filaments propelled by heavy meromyosin (HMM) molecules in the in vitro motility assay were significantly increased ($P > 0.0001$; *SI Appendix*, Fig. S1*D*). These results demonstrate the existence of a functionally intact Ca^{2+}-regulatory system in the isolated native cTFs.

The Structure of Actin Filaments, Reconstituted Actin–Tropomyosin Complexes, and Native cTFs on Mica-Supported Lipid Bilayer Surface. The core of the TFs is formed by double-helical strands of actin subunits. Therefore, actin filaments (F-actin) without Tm–Tn complexes represent a nonregulatory model of TFs, expected to be insensitive to Ca^{2+}. To enable studies of structural modifications induced by Ca^{2+} and myosin in dynamic situations, the actin filaments and TFs must have some degree of freedom for the movement on a substrate. Such flexibility was ensured by using lipid bilayers placed on a mica surface, as previously reported for HS-AFM imaging of F-actin (28). Using a protocol modified in our laboratory (*Materials and Methods*), the actin filaments, reconstituted complexes of actin, tropomyosin, and troponin or native cTFs were deposited on freshly cleaved mica coated with supported lipid bilayers (SLBs). This allowed clear visualization (Fig. 1 and Movies S1–S3) of the right-handed helical filaments with repeating steps (half-helical pitches) and varying peak heights (crossover points of actin double-helix).

A regularly curved strand (highlighted by green in the Fig. 1 *B*–*G* and Movies S1–S3) that complemented the actin helix as well as globular structures (blue arrows in Fig. 1 *C*–*G* and Movies S2 and S3) were observed along the length of reconstituted F-actin–Tm–Tn complexes (*SI Appendix*, Fig. S4 and Movie S2) and native cTFs but not in the bare actin filaments (Fig. 1*A* and Movie S1). The localization of the Tn complex on the one side of cTF seems to indicate a nonsymmetrical configuration of the filaments on the surface in our experimental conditions. However, the Tn complex can be visualized on both sides of regulated actin filaments (Fig. 1 *D* and *E* and Movie S3 *D* and *E*), although transiently at some positions, most likely due to a rotation of the filaments. We noticed that the force applied by the cantilever tip (the AFM probe) is a critical factor for successful imaging of Tm and Tn complexes because of their rather low affinity to F-actin. It is essential that the applied force is not strong enough to break the electrostatic bonds within the regulatory units of the cTFs or reconstituted F-actin–Tm–Tn complex (*Materials and Methods*).

We performed control experiments to certify that the regulatory function of the native cTFs was not disturbed by the AFM probe during scanning, e.g., by causing dissociation of the Tm–Tn complex from the cTFs. In these experiments, HMM was added to the cTFs or to the bare F-actin in the absence of Ca^{2+} and in the presence of 0.5 μM ATP (Movie S4). Under these conditions, the cTF regulatory status (e.g., ref. 25) should, in the absence of disturbances by HS-AFM scanning, largely prevent myosin binding and cycling. In accordance with this view, we found that only few HMM molecules were able to bind to the cTFs but they did not show fast cycling (detachment–attachment); rather, they stayed statically connected to the cTFs with the myosin lever arm mostly in straight position (Movie S4*A*). This is a similar appearance as in the nucleotide-free state (Movie S9). As an additional test to ensure whether HS-AFM scanning does not disturb the cTF regulatory function, one would expect that addition of high Ca^{2+} concentration to the AFM chamber would activate the cTFs with binding of more HMM molecules and appearance of fast detachment–attachment cycling in the presence of ATP. Such behavior with fast cycling and changing binding positions, as well as changes in the lever arm position in several HMM molecules, was observed for cTFs-HMM (Movie S4*B*, presence of high Ca^{2+} and 0.5 μM of ATP, Movie S5) and bare F-actin-HMM (Movie S6, absence of Ca^{2+}, presence of 0.5 μM of ATP), suggesting a state of full activation as expected for a fully functional system.

Analysis of Peak Heights and Half-Helical Pitches of Actin Filaments. Simple quantifications of the actin filament structure based on HS-AFM analysis are given in Fig. 2. These include 1) measurements of the highest points of the peak at the crossover of the actin helix, where the 2 strands of the actin filament are aligned vertically (peak heights; Fig. 2*B*); 2) half-helical pitches as a function of time in the absence of Ca^{2+} (Fig. 2*C*) and the corresponding Gaussian distributions are shown in Fig. 2 *D* and *E*. The peak heights and half-helical pitches of actin filaments in the absence of Ca^{2+} were 9.04 ± 0.63 nm (mean ± SD) and 35.60 ± 5.88 nm, respectively. These values are consistent with previous results from EM (29, 30) and HS-AFM (28) studies (see also analysis of actin filament model PDB:2Y83 made in Chimera; *SI Appendix*, Fig. S3). The addition of Ca^{2+} significantly changed neither the peak height of the bare actin filaments (9.28 ± 0.53 nm), nor the half-helical pitch (37.43 ± 5.41 nm).

HS-AFM Imaging Revealed Changes in the Peak Height Distributions in cTFs at High vs. Low [Ca^{2+}]. The mean peak height of cTFs in the absence of Ca^{2+} was 9.03 ± 0.47 nm (Fig. 3 *A* and *C*), similar to that of bare actin filaments ($P = 0.77$; cf. Fig. 2*D*). Adding 0.1 mM Ca^{2+} into the AFM chamber significantly ($P < 0.0001$) increased the mean peak height to 10.26 ± 1.05 nm (Fig. 3), while also increasing the variance from 4.97 to 10.33% (*F* test, $P < 0.0001$) consistent with increased SD of the height distribution (Fig. 3 *A* and *B*). The time series data in Fig. 3 *A* and *B* suggest that the increased SD of the peak height in the presence of Ca^{2+} is partly due to increased fluctuations of the cTF structure. We attribute this effect to temporal variation in the position of Tm on the cTF surface and/or increased fluctuation in TF structure (giving increased average height) upon binding of Ca^{2+} to Tn-C.

Adding Ca^{2+} to the AFM chamber did not affect the magnitude of the half-helical pitches in the structure of cTFs. This is similar to the effects seen with bare actin filaments. However, despite the presence of Ca^{2+}, the half-helical pitches in the cTFs

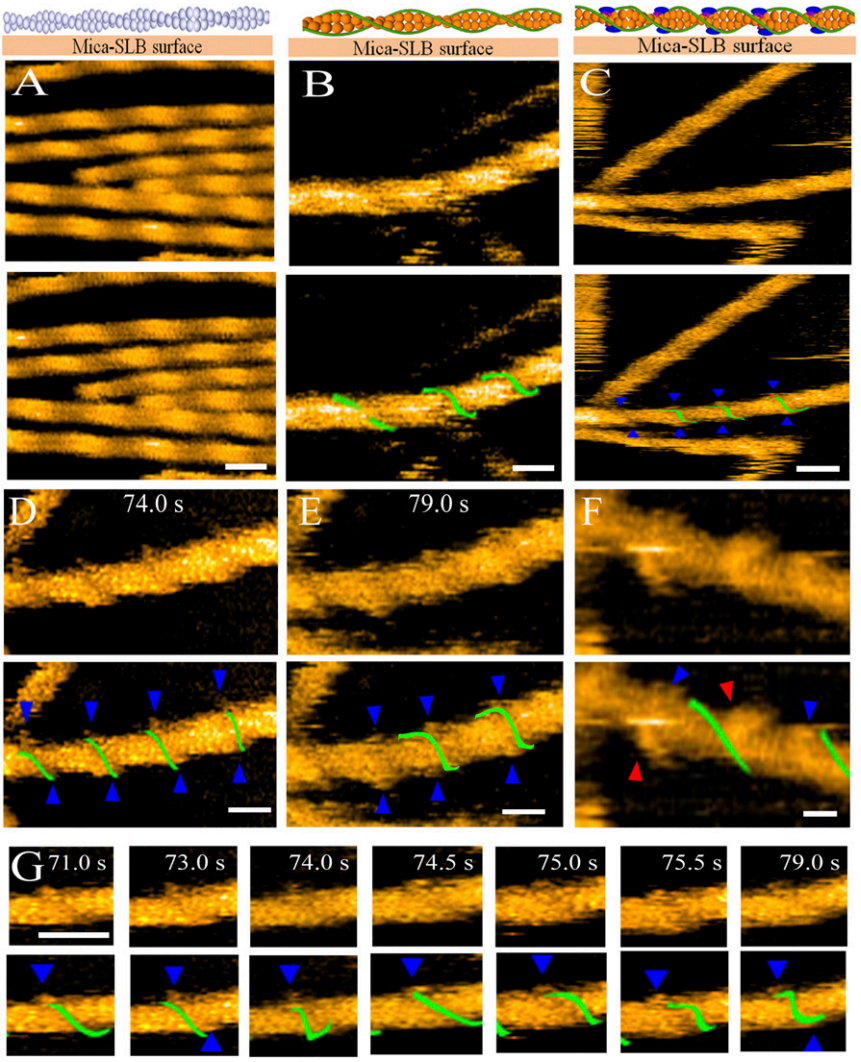

Fig. 1. Structure of actin filaments, reconstituted complexes, and native cTFs imaged by tapping mode HS-AFM in the absence or presence of Ca^{2+} and HMM. (*Top*) Raw image (*A*) or processed by a 2-nm high-pass filter (*B*–*G*). (*Bottom*) Corresponding images, where Tm strands (green lines) and Tn complexes (blue arrows) are shown. (*A*) F-actin filaments (Movie S1*A*). (*B*) Reconstituted F-actin–Tm complex (Movie S1 *B*–*D*). (*C*) Native cTFs (Movie S3 *A*–*C*). (*D* and *E*) Native cTFs at higher magnification in the absence of Ca^{2+} (Movie S3 *D* and *E*) or (*F*) in the presence of Ca^{2+}, ATP, and HMM. The position of Tm strand on the surface of actin filaments is indicated by green lines; the Tn complex and HMM are indicated by blue and red arrows, respectively. (*G*) Sequential HS-AFM images illustrating the dynamics of an individual Tm strand and a Tn complex in cTF regular unit in the absence of Ca^{2+}. Numbers indicate the time frame in seconds. (Scale bars in *A*–*G*: 30 nm.) The scanning area is 200 × 140 nm^2 (*A* and *B*); 200 × 200 nm^2 (*C*); 168 × 63 nm^2 (*D* and *E*); 150 × 75 nm^2 (*F*); 45 × 42 nm^2 (*G*). Scanning rate: 2 fps (*A*–*E* and *G*) and 6.7 fps (*F*). The pixel resolutions are 120 × 84 (*A* and *B*); 200 × 200 (*C*–*G*). *Z* scale: 0 to 10.5 nm. The side view of cartoons for actin, actin–Tm complex, and cTFs with green Tm strand and blue Tn complex are shown for corresponding panel. All raw images are shown in *SI Appendix*, Fig. S2.

are, in general, shorter (33.18 ± 5.79 nm in the absence of Ca^{2+} and 34.68 ± 5.89 nm in the presence of Ca^{2+}) than in the bare actin filament (35.6 ± 5.88 and 37.43 ± 5.41 nm, respectively). This discrepancy in half-helical pitch likely represent the effect of the Tm–Tn complex binding to the surface of actin in TFs, although we did not study this effect in detail. The height distributions for all studied conditions were compared and analyzed by a 1-way ANOVA. There were no statistical differences revealed between F-actin–Ca^{2+} vs. F-actin+Ca^{2+} ($P = 0.96$); F-actin–Ca^{2+} vs. cTFs-Ca^{2+} ($P = 0.63$); and F-actin+Ca^{2+} vs. cTFs-Ca^{2+} ($P = 0.59$). Statistical differences were found for F-actin–Ca^{2+} vs. cTFs+Ca^{2+} ($P = 0.026$); F-actin+Ca^{2+} vs. cTFs+Ca^{2+} ($P = 0.029$); and cTFs-Ca^{2+} vs. cTFs+Ca^{2+} ($P = 0.0071$).

Dynamic Equilibrium of Mean Peak Heights at Low and High Ca^{2+} Depends on the Tm Position on the Surface of cTFs. To validate our findings that Ca^{2+}-induced movement of the Tm–Tn complex on the actin surface relates to height alterations in the structure of cTFs, we explored the processes of cTF activation at different pCa. We measured cTFs peak heights without activation (pCa 9.0), at the Ca^{2+} concentration near the pCa50 (pCa 6.5) according to pCa-ATPase results (Fig. 4*A*), and at high level of activation (pCa 4.5). The mean peak heights along cTFs length were increased from 8.85 ± 1.1 nm at pCa 9.0 to 10.08 ± 0.59 nm at pCa 6.5, and further to 10.91 ± 0.57 nm at pCa 4.5 (Fig. 4*B*).

Considering the pCa-ATPase results (Fig. 4*A*), the mean peak height Gaussian distributions of cTFs in the presence and absence of Ca^{2+} (Fig. 3), and the mean peak height distributions of cTFs at various Ca^{2+} concentrations (Fig. 4*B*), we calculated the height ratio of peaks at pCa 9.0, 6.5, and 4.5 (Fig. 4*C*). The results show that the nonactivated cTFs at low Ca^{2+} (pCa 9.0) are characterized by the prevalence of the peak heights distributed from 6.0 to 9.9 nm, while the Ca^{2+} concentration near the pCa50

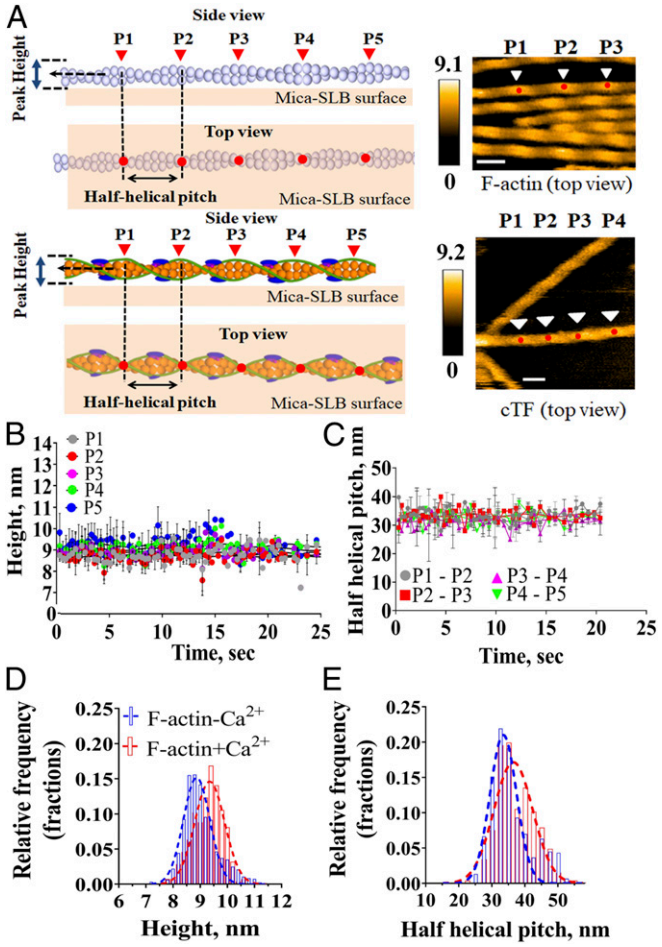

Fig. 2. Analysis of peak heights and half-helical pitches of actin filaments in the presence and absence of Ca^{2+}. (*A*) The peaks (P1–P5) were determined manually, and then the highest points in the center position were automatically searched within a 10 × 10 pixel area. To calculate the peak height, the average heights of the peak were subtracted from the average height of the surface. The abbreviation (P) will be used throughout the paper. The distance between 2 adjusted peaks was calculated as a half-helical pitch. The side and top views of molecular cartoons are shown along with HS-AFM images, where white arrows indicate the peaks and red circles indicate the crossover points in F-actin and cTF. (Scale bars: 30 nm.) The *Z* scale indicates the height range of the F-actin and cTF in the absence of Ca^{2+}. (*B*) Traces of heights in each peak and (*C*) half-helical pitches between peaks of actin filaments in the absence of Ca^{2+} as function of time ($n = 3$, 21 filaments). The peak heights obtained along actin filaments in the absence of Ca^{2+} from P1 to P5 were as follow: P1, 8.80 ± 0.36 nm; P2, 8.69 ± 0.36 nm; P3, 8.81 ± 0.38 nm; P4, 9.00 ± 0.37 nm; P5, 9.17 ± 0.44 nm. Distributions of peak heights (*D*) and half-helical pitches (*E*) of actin filaments in the absence and presence of Ca^{2+}. Gaussian distributions in *D* and *E* were fitted to the data with r^2 of 0.98 and 0.99 in *D*, and 0.99 and 0.98 in *E*, respectively. The scanning was performed in buffer containing 50 mM KCl, 10 mM $MgCl_2$, 20 mM imidazole-HCl, pH 6.0, and 1 mM EGTA or 0.1 mM Ca^{2+}. Number of analyzed peaks in F-actin+Ca^{2+}: (970); F-actin–Ca^{2+} (285).

(pCa 6.5) are characterized by the peak heights distributed almost equally between 6.0–9.9 nm and 10.0–10.9 nm. Last, the peak heights of the activated cTFs at high Ca^{2+} (pCa 4.5) are distributed between 10–10.9 nm (58.2%) and 11.0–12.0 nm (32.0%) with 9.8% in the 6.0- to 9.9-nm range. The height distribution ratios in all these conditions are summarized in Table 1.

The Ca^{2+}-induced changes of peak heights suggest that these structural rearrangements reflect the activation of cTFs through Ca^{2+}-induced movement of Tm on the actin surface. To address this question, we performed HS-AFM experiments where high Ca^{2+} concentration was added to the AFM chamber to track given cTFs in the absence and presence of Ca^{2+}. At the high Ca^{2+} concentration (pCa 4.5), the Tm strand was shifted toward the center (or leftward, if cTFs were located vertically) of the cTFs and the position of Tm was noticeably different at low Ca^{2+} (pCa 9.0) (Movie S7).

We measured the Ca^{2+}-induced swing of Tm on the cTFs surface using discrete Fourier transformation to obtain the amplitude values used to calculate the phase of the Tm wave movement (*Materials and Methods*) and found that, at the high Ca^{2+} concentration, Tm moved ∼17.6° ± 4.5° with 15.19 and 19.97 as the lower and upper 95% confidence intervals of the mean, respectively, from its original position at the low Ca^{2+} (Fig. 4*D*). Thus, a Ca^{2+}-induced increase in the peak height distributions correlates to the Ca^{2+}-induced displacement of Tm on the surface of cTFs.

The Structural Changes of cTFs at Low and High Ca^{2+} Induced by Binding of Myosin Heads in the Presence or Absence of ATP. We performed a series of experiments to study how binding of myosin heads to the cTFs affects the peak height distributions in the nucleotide-free state or in the presence of ATP at low- and high-Ca^{2+} concentrations. We also investigated whether 1 molecule of myosin/HMM is enough to change the position of Tm or Tm–Tn

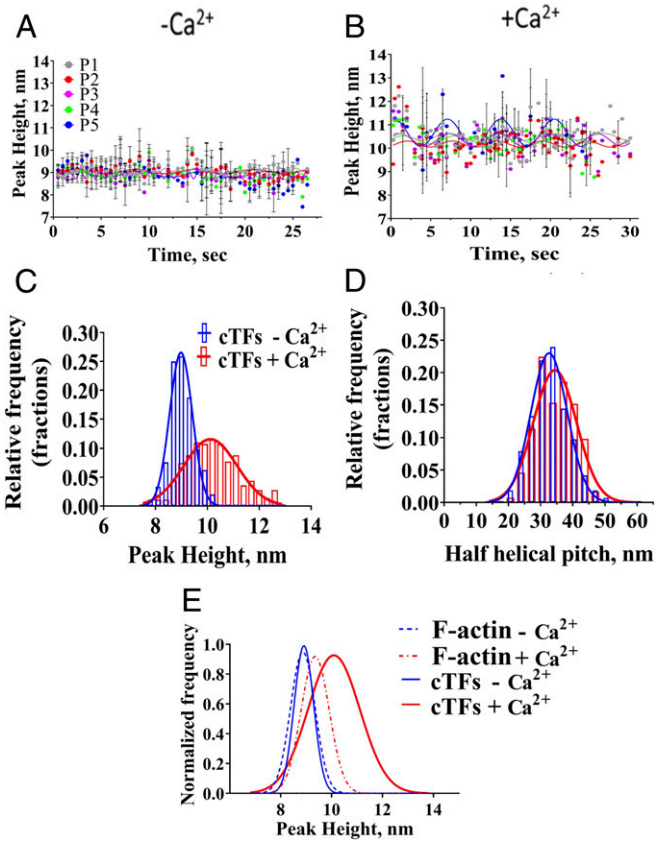

Fig. 3. The alteration of peak heights and half-helical pitches in the structure of regulated cTFs in the presence and absence of Ca^{2+}. (*A* and *B*) Traces of peak heights of cTFs in the absence (*A*) or in the presence (*B*) of Ca^{2+} as function of time. (*C* and *D*) Histograms of peak heights (*C*) and half-helical pitches (*D*) of cTFs in the absence or presence of Ca^{2+}. Frequency distribution data were fitted by Gaussian ($r^2 = 0.97$ and 0.95, respectively); $n = 4$, 18 filaments. (*E*) Normalized Gaussian distributions of peak heights for bare F-actin (no Tm–Tn complex) and cTFs (with Tm–Tn complex) in the presence and absence of Ca^{2+}. Number of analyzed peaks: F-actin+Ca^{2+} (970); F-actin–Ca^{2+} (285), cTFs+Ca^{2+} (777); cTFs-Ca^{2+} (360).

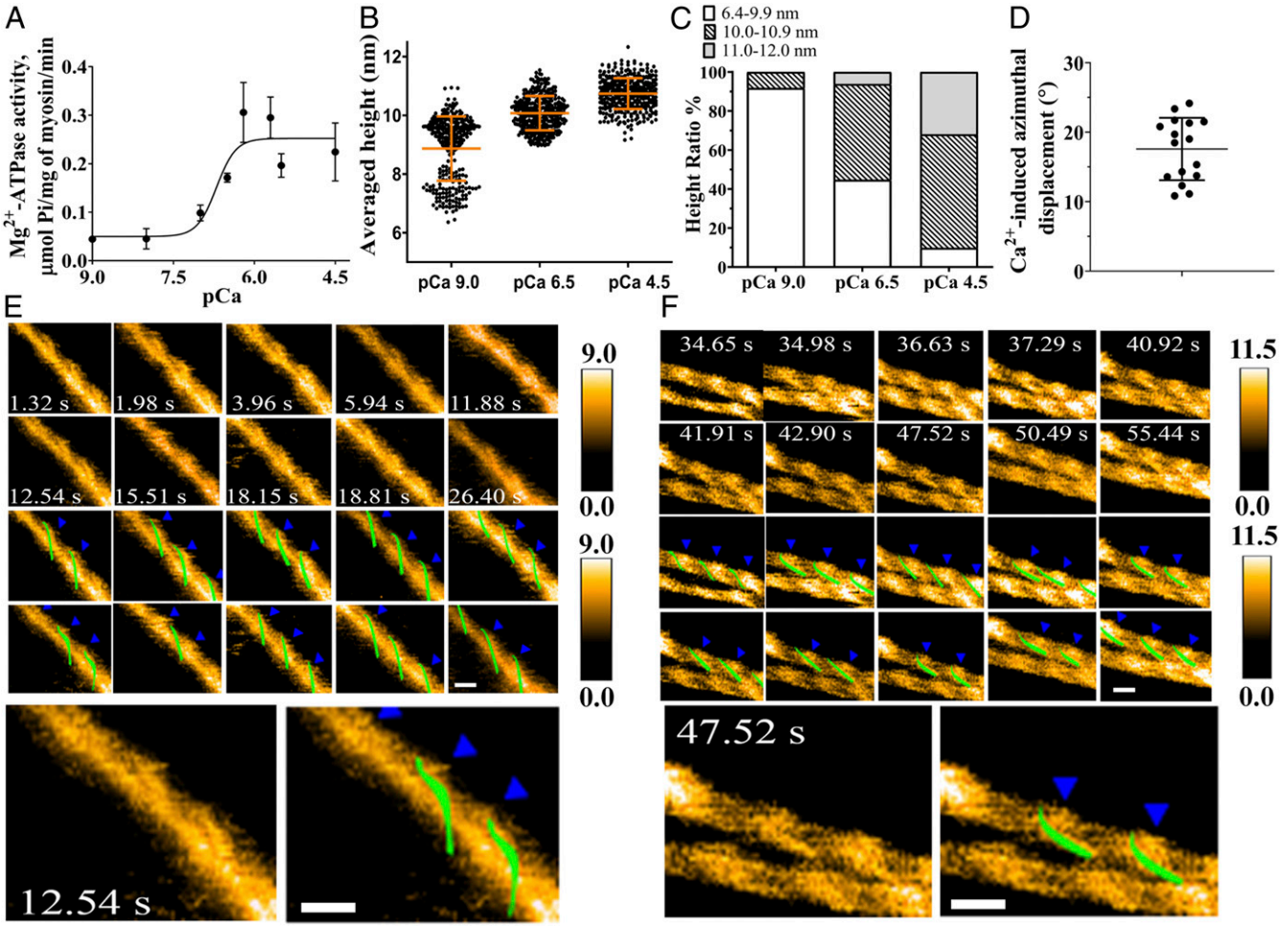

Fig. 4. A dynamic equilibrium of the peak heights in the regulated cTFs at the various Ca^{2+} concentrations. (*A*) The pCa-ATPase relationship of skeletal muscle myosin II and regulated cTFs approximated by the Hill equation (n = 3 independent experiments). (*B*) The peak distributions at the different Ca^{2+} concentrations. (*C*) Percentages of peak heights representing cTFs in the nonactive state at pCa 9.0 (6.4 to 9.9 nm), partly activated cTFs at pCa 6.5 with the level of activation near the pCa50 (10.0 to 10.9 nm), and activated cTFs at pCa 4.5 (11.0 to 12.0 nm). Number of analyzed peaks for pCa 9.0 (294); pCa 6.5 (340); pCa 4.5 (365). Analyzed filaments: n = 30 for pCa 9.0; n = 35 for pCa 6.5; n = 30 for pCa 4.5. (*D*) Ca^{2+}-induced azimuthal movement of Tm (n = 16). (*E* and *F*) Sequential HS-AFM images of native cTFs observed in buffer A at pCa 9.0 (*E*) and pCa 4.5 (*F*). The *Top* shows images processed by 2-nm high-pass filter; the *Bottom* shows the corresponding images with highlighted Tm strands (green lines) and Tn complex (blue arrows). The magnified images show the shift of Tm strand between low and high Ca^{2+}. Note that, for Ca^{2+} conditions (*F*), a second cTF appeared during recording. The scanning area is 150 × 105 nm^2, 80 × 56 pixels, 3 fps. (Scale bars, 30 nm.) Numbers indicate the fame time in seconds. *Z* scale is from 0 to 11.5 nm. Nonprocessed images can be seen in Movie S7.

complex of a regulatory unit (A_7–Tm–Tn) to fully activate TFs from the B- or C-states to the M-state in that and possibly neighboring units.

The height distribution profile of the cTF segments with and without bound HMM molecules (Fig. 5 *A* and *B* and Movie S8) showed that height is increased at the site of cTF–HMM interaction. This observation is consistent with the height measurements. The weak (presence of ATP and Ca^{2+}) and strong (absence of ATP) binding of myosin heads to the regulated cTF caused an overall increase of the cTFs peak heights as shown by the Gaussian distributions shifted to the right if compared with conditions where no HMM was added (Fig. 5 and Table 2). However, comparison of the peak distributions among the conditions where HMM was added (Fig. 5 *E*–*I*) revealed different height profiles. In the rigor conditions at low Ca^{2+} and in the presence of 1 U/mL apyrase, which was used to remove any traces of ATP and ADP, the HMM is tightly bound to the cTFs (Movie S9) and the Gaussian distributions showed a broad peak height profile (Fig. 5*E*, black curve). In contrast, binding of myosin to bare actin filaments observed in rigor conditions showed a height profile similar to that of cTFs in the B-state (Fig. 5*I*, orange curve, and *SI Appendix*, Fig. S6).

At low-Ca^{2+} and high-ATP conditions, HMM is weakly bound to the cTFs, and the height distributions shifted to the much narrower profile (Fig. 5 *G* and *I*, magenta curve; Movie S11). Surprisingly, the similar narrow profile was found for the conditions when HMM was added in the presence of high Ca^{2+} in the nucleotide-free state, i.e., in the presence of 1 U/mL apyrase

Table 1. Peak heights distributions ratio in cTFs observed at low-Ca^{2+} (pCa 9.0), medium-Ca^{2+} (pCa 6.5), and high-Ca^{2+} (pCa 4.5) conditions

	Peak height distributions ratio, %		
Peak heights, nm	pCa 9.0	pCa 6.5	pCa 4.5
6.0–9.9	91.8 (B-state)	44.7 (B-state)	9.8 (B-state)
10.0–10.9	8.2 (C-state)	49.1 (C-state)	58.2 (C-state)
11.0–12.0	0 (M-state)	6.2 (M-state)	32.0 (M-state)

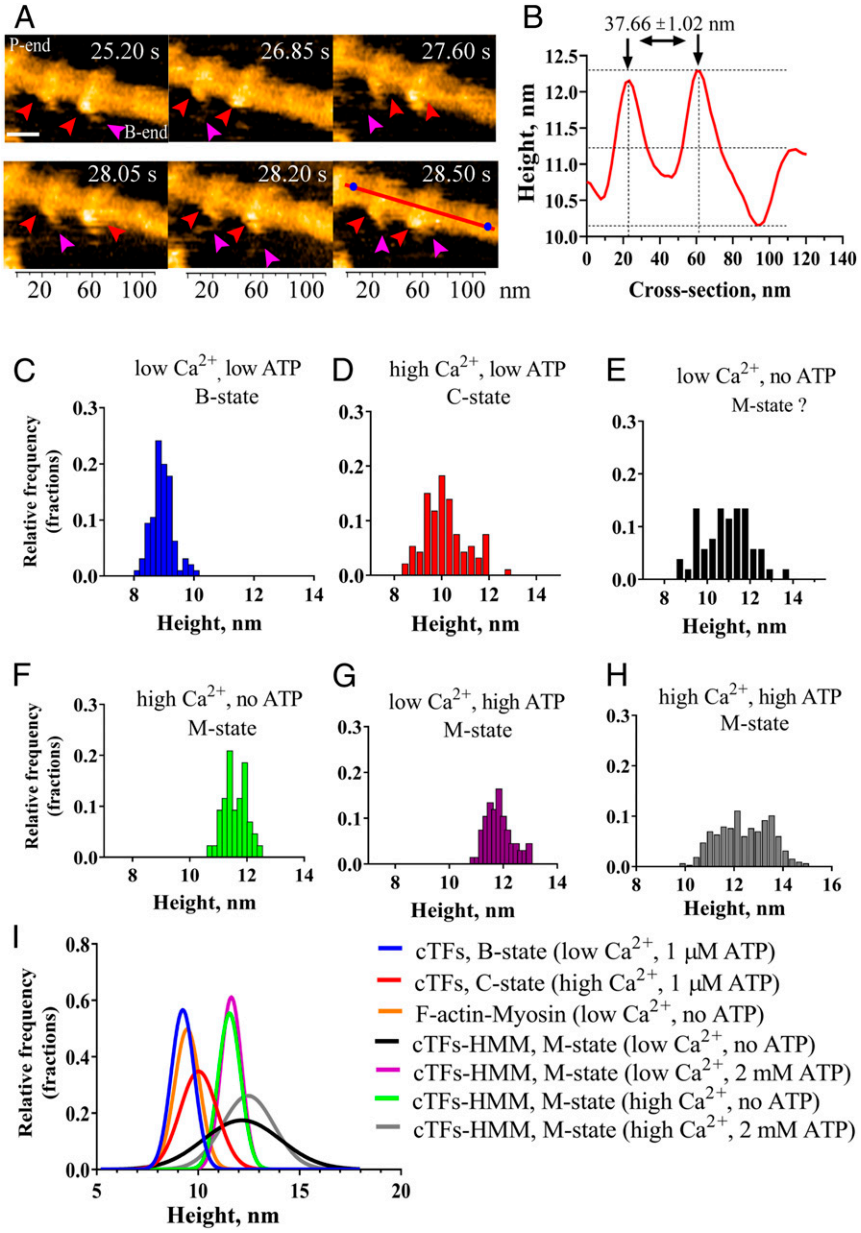

Fig. 5. Height distributions of cTFs in the B-, C-, and M-states. (*A*) Sequential HS-AFM images of cTFs with bound HMM (myosin heads shown by red arrows; myosin neck and lever-arm shown by magenta arrows) in the presence of high Ca^{2+} and 0.5 μM ATP. (Scale bar, 30 nm.) Numbers on the frames indicate the time in seconds. The filament polarity determined from the position of bound HMM heads (Movie S8); (*B*) The height distribution profile of cTFs (n = 3, 90 frames). The mean center positions in cTFs are indicated by blue dots. The red line indicates the cross-section used for the height distribution analysis. The black arrows show the peak occurred at HMM binding (~20 and 60 nm). (*C–H*) Histograms of peak heights at low (pCa 9.0) and high (pCa 4.5) calcium concentration and at micromolar and millimolar [ATP]. (*I*) Gaussian distributions for all studied conditions. For nucleotide-free condition, 1 U/mL apyrase was added. Note an overall shift in the positioning toward higher peak heights from the B-state to the M-state. Related to Movies S9–S12. The histograms were fitted by Gaussian function with r^2 = 0.99 (blue curve), r^2 = 0.95 (red curve), r^2 = 0.84 (black curve), r^2 = 0.99 (green curve), r^2 = 0.99 (orange curve), r^2 = 0.97 (gray curve), and r^2 = 0.99 (magenta curve), respectively. Number of peaks analyzed: 151 (*C*), 93 (*D*), 94 (*E*), 65 (*F*), 105 (*G*), and 315 (*H*).

(Fig. 5 *F* and *I*, green curve; Movie S10), that represented strongly bound HMM to the cTFs. These results suggest that the weak and strong bound myosin heads shifted the peak height distributions to the similar degree (Fig. 5*I*, green solid and magenta curves), although the mechanism of the shift could be different, as discussed later.

For the condition of fully activated cTFs, i.e., in the presence of high Ca^{2+}, high ATP, and myosin, the Gaussian distribution showed the broad height profile (Fig. 5 *H* and *I*, gray curve). At these conditions, myosin heads are cycling and bound to the cTFs transiently (Movie S12). Interestingly, the height distribution is similar to that observed under rigor conditions (Fig. 5 *E* and *I*, black curve) when HMM is strongly bound to TFs (Movie S9). The mean values of the peak heights at each condition obtained from corresponding Gaussian distributions are summarized in Table 2.

The data presented here support our idea that the wide range of different heights related to the different positions of Tm–Tn complexes along cTF length. Overall, the range of different heights in the presence of HMM might be related to complex local and propagating effects on cTF height of myosin binding under the different conditions. At the segments where HMM is

Table 2. Mean values of peak heights in the structure of regulated cTFs in B-, C-, and M-states

	Averaged peaks, nm						
Variables	cTFs, B-state, [−Ca^{2+}] [1 μM ATP]	cTFs, C-state [+Ca^{2+}] [1 μM ATP]	F-actin + Myosin [−Ca^{2+}] [−ATP]	cTFs+HMM [−Ca^{2+}] [−ATP]	cTFs+HMM M-state [−Ca^{2+}] [2 mM ATP]	cTFs+HMM M-state [+Ca^{2+}] [−ATP]	cTFs+HMM, M-state [+Ca^{2+}] [2 mM ATP]
Mean	9.03	10.26	9.55	11.99	11.55	11.59	12.43
SD	0.47	1.05	0.42	1.59	0.36	0.40	1.07
SEM	0.022	0.055	0.06	0.16	0.04	0.06	0.06

Concentration of ATP used: 1 μM for TFs in the B- and C-states, and 2 mM for the M-state in the presence of high Ca^{2+} (pCa 4.5).

bound the height is higher, at the segment where HMM is not bound the height is lower. Also, at 2 mM ATP HMMs constantly detach and reattach, which also contributes to the height distribution.

Discussion

Application of HS-AFM to Study cTFs Dynamics. We used a HS-AFM to study the dynamics of native cTFs under relaxing (absence of Ca^{2+}) and activating (presence of Ca^{2+}) conditions and in the presence of strongly and weakly bound myosin to reveal the mechanism of cTF regulation through Tm movement. Although the structure of actin and its complex with Tm or Tm–Tn has previously been extensively studied by X-ray diffraction (7, 8, 16, 18), EM (9, 10, 20, 22, 30–33), and cryo-EM (23–25, 34, 35), one of the largest advantages of using HS-AFM is the ability to observe the protein structure and protein interaction in physiological solutions in x, y, and z directions without sample processing. With an image acquisition rate of ∼100 to 500 ms/frame (3 to 10 frames per second [fps]), we can achieve a spatial resolution in the range of 1 to 5 nm in the horizontal direction and 0.15 nm in the vertical direction of the plane of analysis (36, 37). This degree of spatial resolution in 3 dimensions is unprecedented in studies of dynamic changes in the structure of TFs, actin, myosin, and their complexes upon relaxation and activation.

Therefore, in contrast to techniques relying on averaging and/or fixation of the preparation in various ways, the HS-AFM movies directly show the fluctuations of individual Tm (Movie S3). This, as well as low but nonzero TF-activated ATP turnover rate in the absence of Ca^{2+} (ref. 25 and Movie S4*A*), is consistent with mobility of Tm on the cTF surface also in the blocked state. Such mobility is also indicated by the time series in Fig. 1*G* (Movie S3*F*), suggesting sufficient displacement of Tm in the center of a regulatory unit (between 2 Tn molecules) to expose isolated myosin binding sites. It is of interest to note in this connection that up to 4-nm displacement of the center of the Tm molecule by bending between the Tn pinning points (at 36-nm separation) would correspond to an elastic bending energy of only ∼2 k_BT, assuming an effective persistence length of Tm of 500 nm (21).

HS-AFM Imaging Revealed Two Distinct Average Positions of Tm on the cTFs Surface at Low- and High-Ca^{2+} Concentrations. We found that the heights of the peaks that correspond to the actin crossover points in the structure of cTFs are changed by increased concentrations of Ca^{2+}. This result is reminiscent of the alteration of height as function of Ca^{2+} binding to the calmodulin previously observed in HS-AFM experiments and attributed to substantial conformational changes (38). We assumed that the lowest peak height at the lowest Ca^{2+} concentrations matches the blocked B-state, while the highest peak at the high Ca^{2+} and absence of myosin matches the closed C-state of cTFs. To certify that altered heights correlate with transition between functional states of the cTFs, we performed several independent measurements. First, we compared the peak height distributions of bare actin filaments (no Tm–Tn) and cTFs (with Tm–Tn) in the absence of Ca^{2+}. We found that, in the absence of Ca^{2+}, the height distribution observed for the bare actin filaments is very similar to that of cTFs in the absence of Ca^{2+} (Figs. 2 and 3), consistent with an early X-ray diffraction study (39). Taking these findings together, in the absence of Ca^{2+}, the Tm strand is located at the edge of the actin groove, and this position does not affect the height distribution between bare actin filaments and cTFs, suggesting that this state matches the blocked, nonactivated B-state of cTFs.

To study whether the height distribution at the low and high Ca^{2+} is altered due to Ca^{2+}-induced movement of Tm, we attempted to observe the Tm strand on the surface of cTFs. To the best of our knowledge, the imaging of Tm on the surface of native TFs without any fixation agents or freezing in a hydrated medium was not performed. In a previous HS-AFM study, Tm has been visualized in a reconstituted F-actin–Tm complex (40), but in this case the complex was fixed by phalloidin and glutaraldehyde, and the acquisition rate was about 20 to 30 times slower than used here. According to our data, Ca^{2+} induces movement of the Tm strand on the TF surface corresponding to an azimuthal angle of 17.6° ± 4.5° with 15.19 and 19.97 as the lower and upper 95% confidence intervals of the mean, respectively. This differs from results obtained previously by EM of negatively stained TFs, where the Ca^{2+}-induced movement of Tm amounted to ∼20° to 25° (9, 27) and ∼30° (10). The analysis of TFs segments revealed that the Tm strand displacement depends on localization of Tm repeats and ranges from ∼18° to ∼28° (22). Our results are in close agreement with recently reported data for the native cTFs collected using cryo-EM, where Tm was moved ∼15° at the high Ca^{2+} on the TF surface (25). A difference of the mean value in Tm shift between our HS-AFM data and cryo-EM data most likely relates to a nonstatic position of Tm on the surface of cTFs, and the fact that we are not averaging the HS-AFM images used for analysis. Another reason for the difference may be that even at high Ca^{2+} concentrations not all Tm are moved to the position where weak binding of myosin occurs. Most importantly for our analysis, the movement of Tm on the cTFs surface is closely related to the alteration of the peak heights.

We noticed that the peak heights, and therefore the Tm position on the surface of cTFs, could be changed within a wide range depending on the experimental conditions. At the low-Ca^{2+} concentrations (pCa 9.0), the range of peak heights fluctuated from 6.4 to 10.9 nm. The likely explanation of this finding is that Tm is not statically fixed on the TF surface, but it moves to cause rearrangements of Tn-T and Tn-I subunits, contributing to the increases in the peak heights. This interpretation fits well with EM and cryo-EM data showing that ∼75 to 80% of the cTFs are found in the B-state configuration at low-Ca^{2+} concentrations, whereas ∼20 to 25% of TFs segments are in the C-state (25, 27). In the EM analysis, short TF segments were treated as single particles causing ∼20% of the segments to exhibit unexpected configuration at the given condition of either low or high Ca^{2+} (27). Single-particle analysis is similar to our analysis of tracking peak height distribution in each cTF's peak (actin crossover helix) or functional unit in small areas from 100 × 100 to 400 × 400 nm^2. According to peak distribution data

(Figs. 3 and 4 and Table 1), the calculated height ratios show the presence of 3 distinct peak populations in the structure of cTFs: 1) ∼6.4- to 9.9-nm peaks: the majority of these peaks were found under relaxing conditions (pCa 9.0), consistent with representation of the blocked or B-state of TFs; 2) ∼10.0- to 10.9-nm peaks: these peaks were found either at the pCa 6.5 or activating (pCa 4.5) conditions representing the closed or C-state of TFs; and 3) ∼11.0- to 12.0-nm peaks: these peaks were observed mostly under activating conditions (pCa 4.5). The majority of these and higher peaks were observed under fully activating conditions in the presence of Ca^{2+}, ATP, and myosin (the M-state; Fig. 5, Table 2, and Movie S12).

A population of ∼92% of the cTFs at pCa 9.0 was found in the blocked state, while a population of ∼8% was found in the activated state. Within these "activated" segments of the cTFs, Tm is not blocking the myosin binding sites, and myosin is therefore able to attach to the cTFs, explaining why myosin is able to activate TFs even at low-Ca^{2+} concentrations (41). At pCa 6.5, the portion of the high peaks (10.0 to 10.9 nm) is increased to ∼49%, while the portion of low peaks (6.4 to 9.9 nm) still constitute ∼45% (Fig. 4 *B* and *C*). These ratios mirror the c-open and c-blocked states proposed by Risi et al. (25). The pCa 6.5 is also characterized by the presence of ∼6% of the highest peaks (11.0 to 12.0 nm), which likely represent the open or myosin states of cTFs. Indeed, at the high-Ca^{2+} concentration, the majority of the peaks are characterized by the C-state (∼58%), and the open or M-state (∼32%), while ∼10% of the peaks represent the B-state (Figs. 4 and 5 and Tables 1 and 2).

Taken together, our data from direct observation of cTFs under near-physiological conditions show a dynamic equilibrium of activated and inactivated segments along the cTF's length, in a ratio that changes dynamically depending on the Ca^{2+} concentration. This is consistent with indirect evidence from EM studies (22, 25), and spectroscopic studies in solution of large TF ensembles (11, 14, 15) and binding of fluorescent myosin to isolated TFs to report activation level (42). The data also seem to suggest enhanced thermal fluctuations of cTFs in the presence of Ca^{2+} as shown by increased variance of cTFs+Ca^{2+} vs. cTFs-Ca^{2+} (Fig. 3 *A* and *B*). Thus, the increased height in the presence of Ca^{2+} and upon myosin binding might be attributed to a freely moving Tm and rearrangements of Tn-T and Tn-I subunits on the cTF surface. However, it may also be of relevance to consider evidence for reduced persistence length of the TF of skeletal muscle when Ca^{2+} binds to Tn (43), suggesting a generally more flexible filament with possible conformational changes in actin. In accordance with that view, some authors (e.g., ref. 44) have considered structural changes in the actin filament as a result of Tm interactions (see also ref. 45), and there is evidence that myosin binding to actin causes structural changes in the filament (39, 44, 46) manifested by reduced persistence length and changes in single-molecule fluorescence resonance energy transfer data suggesting intrasubunit structural changes.

Strong and Weak Myosin Binding Induces Similar Changes in the Structure of cTFs. The interaction of HMM with cTFs caused an increase in the peak height distributions (Fig. 5*B* and Movies S9–S12). Most importantly, such changes were observed both in the absence and presence of Ca^{2+}, and in the absence and presence of ATP, i.e., induced by the weak and strong binding of myosin heads to the cTFs either in B- or C-states. In our experiments, the presence of ATP would produce primarily weakly bound myosin states (with ATP or ADP and inorganic phosphate at the active site), while the absence of ATP leads to strongly bound myosin heads (47). Under the variety of conditions used in our experiments, the fractions of all bound myosins are different; for example, the fraction of bound myosins at high ATP is appreciably lower than in the absence of ATP (46). However, we only analyzed events where a myosin (HMM) molecule was observed, thus avoiding this complication.

In our analysis, the M-state is characterized by increase of the peak heights, i.e., a right shift of the Gaussian height distribution (Fig. 5 and Table 2). Depending on the specific conditions, the shift in peak heights upon binding of myosin ranged from 1.43 to 2.3 nm (Table 2). The myosin heads bound to cTFs add a contribution to the height profile. However, this contribution is in the range of ∼1.0 and 1.4 nm if the cross-section is measured through the HMM or less than ∼1.0 nm if the cross-section is measured through the middle of cTFs (Fig. 5*B* and *SI Appendix*, Fig. S5*F*). Thus, the difference in height between B-, C-states and M-state (Table 2) is determined not only by the contribution of the myosin head dimensions, but also by Tm movement toward the center of the actin filament induced by myosin binding. It is of interest to note that these numerical values are very similar to the shift of Tm of 1.0 to 2.3 nm observed in cryo-EM studies upon myosin binding to TFs in the closed state (25, 48).

In the rigor conditions (low Ca^{2+}, no ATP), HMM is strongly bound to the cTFs without detachment/attachment (Fig. 5*I*, black curve; Movie S9) and a broad height profile in the Gaussian distribution was observed. The reason for this may be that cTFs are in the B-state at low Ca^{2+}, representing a mix of segments in the blocked and closed states with the prevalence of the blocked segments. Thus, if HMM is strongly bound to the cTF segments that are in the blocked configuration, it moves the Tm strand to the closed state, while ∼8% of segments in closed-state configuration moved to the M-state. Similar wide range of intensity profiles was observed when myosin bound to the TF at low ATP (0.1 μM) and pCa 6.0 (42). This rearrangement makes it possible that the adjacent blocked segments around the site of HMM–cTF interaction also move to C- and M-state. It was shown previously (14) that strong binding of a myosin head to the regulatory TF is enough to effectively switch 10 to 12 neighboring actin monomers, i.e., approximately 2 A_7–Tm–Tn units.

When HMM was strongly bound to cTFs at high [Ca^{2+}] in the absence of ATP (Fig. 5 *F* and *I* and Movie S10), a narrow and right-shifted Gaussian distribution curve was obtained (Fig. 5*I*, green curve). Here, the strongly bound myosin heads are interacting with cTFs in the C-state (which is the mix of TF segments in the closed and open states with the prevalence of closed one) and, by analogy, switching the Tm strand to a canonical M-state observed in EM studies (refs. 10 and 22; reviewed in ref. 49). When HMM was weakly bound to cTFs at low [Ca^{2+}] and in the presence of high [ATP] (Fig. 5 *G* and *I*, magenta curve; Movie S11), a similarly narrow and right-shifted peak height Gaussian distribution profile was observed, like in the presence of high [Ca^{2+}] and absence of ATP. Here, at the low Ca^{2+}, the binding of HMM is prohibited by presence of high ATP and B-state cTFs. As discussed, the B-state is a mix of TF segments in blocked and closed states having ∼8% of the segments in the closed configuration, that is structurally similar to closed configuration (Fig. 4 and Table 1). At low [Ca^{2+}] and high [ATP], weakly bound HMM was not able to make the local rearrangement of the adjacent blocked segments as strongly bound HMM, which explains the narrow profile.

Finally, if we consider the condition where HMM is bound to cTFs in the presence of high [Ca^{2+}] and high [ATP], the broad Gaussian distribution profiles were observed (Fig. 5 *H* and *I*, gray curve; Movie S12). Here, 2 processes may happen in parallel: 1) the movement of the Tm strand to the canonical M-state positions during the cycling stages when HMM is strongly bound to TFs coupled with the lever arm movement after Pi release, and 2) the Tm strand moved back when HMM is weakly bound to cTFs during few ATPase cycle stages with weakly bound actomyosin states.

Conclusions

A key finding of the present study is that the binding of a single myosin motor to TFs during active ATP turnover at near-physiological [MgATP] conditions produce a similar activating effect on the TF, albeit only locally, as the binding of myosin to TF in the absence of MgATP. The data suggest the possibility of local transient exposure of myosin binding sites both by binding of myosin at high ATP concentration and in the absence of Ca^{2+} and myosin. In addition to the above evidence for localized cTFs activation, our study also provides evidence overall confirming the canonical mechanism of TF activation by Ca^{2+} and strong myosin binding predicted by previous spectroscopy and cryo-EM methods (11, 21, 24, 25, 42, 48). We visualized the dynamical displacement of individual Tm strands in the center of a regulatory unit of cTF (between 2 troponin complexes) to expose isolated myosin binding sites at the relaxed and activation conditions. The displacement of Tm at the relaxed conditions was suggested in several studies but had never been visualized. This finding explains the ability of myosin binding to TF at the relaxed conditions.

Materials and Methods

Proteins. Native cTFs were purified from rabbit right and left ventricular cardiac glycerinated muscle following a protocol of Snook et al. (50) with some modifications described in *SI Appendix*. Actin was purified from acetone powder of rabbit skeletal muscle (Sigma-Aldrich) according to a protocol (51). Myosin was purified from rabbit psoas muscle as described (52). HMM was prepared by proteolysis of the myosin with α-chymotrypsin (Sigma-Aldrich) according to protocols described here (53).

Lipid Bilayer Template for HS-AFM Imaging. We tested several surfaces, including glass and mica, to be used during the HS-AFM experiments. We found that mica-SLB is the best one for actin and TF imaging as well for TF–myosin II interaction. Mica disks (1.5 mm in diameter; RIBM) were glued on the top of glass cylindrical sample stage and freshly cleaved before depositing lipids. The positively charged lipid bilayer was prepared according to Uchihashi et al. (54) with several modifications. Briefly, 1,2-dipalmitoyl-*sn*-glycero-3-phosphocholine (DPPC) (Avanti Polar Lipids) and 1,2-dipalmitoyl-3-trimethylammonium-propane (DPTAP) (Avanti Polar Lipids) in 100% chloroform were mixed at a weight ratio 9:1 or 9.5:0.5, dried from organic solvent with warming up to 45 °C, and dissolved to 2 mg/mL by solution, containing 50 mM KCl, 4 mM $MgCl_2$, 0.5 mM EGTA, 25 mM imidazole-HCl, 1 mM DTT, pH 6.0 (buffer A). The mix then was vortexed, sonicated to disperse the lipids for 2 to 4 min, and subjected to snap freezing in liquid N_2 and thawing (5 cycles). Lipids were then aliquoted and stored at −80 °C. Before use, the aliquot was diluted five times by 10 mM $MgCl_2$ (to 0.4 mg/mL lipid solution) and sonicated again for 2 min. Lipids were placed on the top of freshly cleaved mica and incubated at room temperature in the humid chamber to prevent drying the lipids for at least 30 min or overnight.

HS-AFM. We used the newest version of the HS-AFM developed by Ando et al. (36) and commercialized by RIBM, equipped with high-speed scanner and proportional, integral, and derivative (PID) feedback control system. HS-AFM imaging was observed in tapping mode by using Olympus microcantilevers with silicon nitride tip and radius of 24 nm (BL-AC10DS-A2; RIBM) or with carbon tip fabricated by electron beam deposition and sharped by plasma etcher (Kanazawa University; ref. 55) with the following parameters measured in liquid: spring constant between 0.08 and 0.15 N/m, quality factor (*Qc*) of 1.4 to 1.6, and resonant frequency of 350 to 650 kHz. To be able to visualize the Tm and Tn complex on the surface of F-actin, the applied force of AFM probe must be taken with care to avoid applying too high force that might break the electrostatic bonds between the proteins. The force applied by the cantilever's AFM probe is given by the following equation (from ref. 55):

$$F = \frac{K_c}{2Qc}\sqrt{A_0^2 - A_{sp}^2}, \quad [1]$$

where A_{sp} is the reference oscillation amplitude when AFM probe approached to the surface; A_0 is the free oscillation amplitude; k_c is the spring constant of the cantilever; and Qc is the quality factor of cantilever. The applied forces were in the range of 15 to 20 pN (actin and cTF imaging). The values represent a maximal range that was calculated from the cantilever's force curve. For imaging the actin–myosin complex during weak interaction, the tapping force was reduced by setting A_0 at 2 nm and A_{sp} set close to the A_0, thus reducing the tapping force more than 80% to reach only ∼3 to 10 pN.

HS-AFM imagining of F-actin and cTFs in the absence or presence of Ca^{2+} and 0.5 to 1 μM of ATP was performed in the following ways. A concentration of 1.5 μM of F-actin (drop 3.0 μL) was placed on the mica-SLB for 10 min under a wet chamber after which the unbound filaments were washed out by the buffer A or solutions with low (pCa 9.0) or high (pCa 4.5) Ca^{2+} concentrations. To reconstitute F-actin–Tm or F-actin–Tm–Tn complexes, 2.8 μL of 1.5 μM F-actin was placed on the mica-SLB for 10 min as above. After wash by buffer A with appropriate Ca^{2+} concentration, then 3.0 μL of 1.5 to 5 μM of porcine Tm (Sigma-Aldrich) or bovine cardiac Tm–Tn complex (Cytoskeleton) were added to the F-actin filaments bound to the mica-SLB surface, and complexes were incubated for additional 10 min under the wet chamber. Finally, unbound complexes were washed out by the buffer A.

The dynamic alterations in the cTF structure induced by Ca^{2+} were imaged as follows. First, 2 to 20 μL of B-state cTFs (0.01 mg/mL) in buffer A were placed on the top of mica-SLB surface and incubated for 10 min in the wet chamber. The unbound cTFs were washed out by the buffer A, the Z-scanner with sample was installed, and HS-AFM imaging was performed. To visualize the dynamical changes in cTF structure from the B- to the C-state, 0.1 mM $CaCl_2$ (pH 6.0) was injected directly into the AFM chamber. To avoid damage of the *Z*-scanner and cantilevers, the scanning was stopped before injection of Ca^{2+}; however, in some cases, the injection was made during the scanning to analyze the same filaments before and after injection.

To measure the conformational changes of cTFs at different Ca^{2+} concentrations, solutions with low-Ca^{2+} (pCa 9.0) (equal to $-\log[Ca^{2+}]$), moderate-Ca^{2+} (pCa 6.5), and high-Ca^{2+} (pCa 4.5) concentrations were prepared. The Maxchelator online software was used to calculate the free Ca^{2+} concentration (https://web.stanford.edu/~cpatton/CaEGTA-TS.htm). The procedure for imaging was similar to that explained above; the unbound cTFs were washed out by the pCa 9.0 buffer and attached to the mica-SLB surface; thereafter, cTFs in the B-state were imaged. Then, the pCa 9.0 buffer was replaced by the pCa 6.5 or pCa 4.5 buffers. To visualize the effect of Ca^{2+} on the peak heights and the half-helical pitch amplitudes, the sine wave function was applied: Y = Baseline + Amplitude*sin(Frequency*X + Phase shift), where the wavelength = (2*pi)/Frequency.

HS-AFM imagining of cTFs at low-Ca^{2+} (pCa 9.0) or high-Ca^{2+} (pCa 4.5) concentrations in the presence of skeletal HMM was performed in the following way. Two to 20 μL of TFs (0.01 mg/mL) in the buffer A (relaxing conditions, absence of Ca^{2+}) were placed on mica-SLB surface for 10 min in the wet chamber and unbound cTFs were removed by exchanging for the buffer B, containing 25 mM KCl, 2 mM $MgCl_2$, 1 mM EGTA, 20 mM imidazole, 1 mM DTT, pH 7.0. Then, 2 to 20 μL of skeletal HMM (0.0035 to 0.01 mg/mL, 7 to 20 nM) in buffer A (in some cases, containing additional 50 mM KCl) was placed on top of the mica-SLB surface with bound cTFs for 10 min in the wet chamber. Unbound HMM was washed out by buffer B followed by washing several times with appropriate buffer B with low- or high-Ca^{2+} concentrations containing 0.5 μM, 1 μM, or 2 mM of ATP. The HS-AFM chamber was filled with the solutions matching to the experimental conditions. To confirm nucleotide-free conditions, 1 U/mL apyrase (Sigma-Aldrich) was added to remove traces of ATP and ADP.

Data Analysis and Processing of HS-AFM Images. The HS-AFM images were analyzed by Kodec software (version 4.4.7.39) (28). We performed "height analysis" to determine the peak heights and half-helical pitches between adjustment peaks in the structure of actin and cTFs under different conditions, as follows. We first checked original *Z*-scale parameters with minimum and maximum heights corresponding to voltage values from −5 to +5 V (analog-to-digital conversion). We then applied a low-pass filtering to remove spike noise from the analyzed image to make the *xy*-plane flat. The position of peak in actin and cTFs were first determined manually, and then the highest points within the crossover actin helix were automatically searched within the 10 × 10 or 5 × 5 pixel area. To calculate the peak height, the average height of the center of mass of the filaments was subtracted from the average height of the surface. Half-helical pitches (a distance between center of 2 adjustable peaks) were also used to characterize conformational changes in the structure of F-actin, F-actin–Tm, F-actin–Tm–Tn complexes, and native cTFs.

To calculate Ca^{2+}-induced movement of the Tm on the cTFs surface at the low and high Ca^{2+}, a discrete Fourier transformation of the HS-AFM images of cTFs under these conditions was performed in the Fijj software (IJ 1.46r; NIH). It results in a stack of the real and the imaginary parts of the Fourier spectrum. The obtained *x*,*y*-coordinates of the point selection (where Tm is seen on the HS-AFM images) as well as the corresponding real and complex

amplitude values were used to calculate the phase of the Tm wave movement using the following equation:

$$\text{arctangent}(x) = \frac{x_{im}}{x_{rl}}, \quad [2]$$

where arctangent of x is defined as the inverse tangent function of x when x is real; x_{im} and x_{rl} are the imaginary and real parts of the Fourier spectrum, respectively.

Unless stated, HS-AFM imaging was performed at 2 fps (500 ms) or 6.7 fps (150 ms). Data analysis and statistics, Gaussian distributions, and data fitting were performed in GraphPad Prism software (version 7). Values are reported as mean ± SD. A level of significance of $P \leq 0.05$ was set for all analyses. Some images were processed by high-pass filter using IgorPro software (version 6.3.7.2; WaveMetrics), as indicated in the figure legends.

ACKNOWLEDGMENTS. This work was supported by the Natural Science and Engineering Research Council of Canada (to D.E.R.) and Canada Foundation for Innovation (to D.E.R.), and partly supported by Extramural Collaborative Research Grant of Cancer Research Institute, Kanazawa University (to O.S.M.). A.M. was supported by the Swedish Research Council (Grant 2015-05290) and the Faculty of Health and Life Sciences of Linnaeus University. D.E.R. is a Canada Research Chair in Muscle Biophysics. We thank Profs. Ando and Kodera (Kanazawa University) for useful comments and valuable advice for acquisition and analysis of the HS-AFM data.

1. J. A. Spudich, H. E. Huxley, J. T. Finch, Regulation of skeletal muscle contraction. II. Structural studies of the interaction of the tropomyosin-troponin complex with actin. *J. Mol. Biol.* **72**, 619–632 (1972).
2. W. Lehman, R. Craig, P. Vibert, Ca^{2+}-induced tropomyosin movement in *Limulus* thin filaments revealed by three-dimensional reconstruction. *Nature* **368**, 65–67 (1994).
3. S. E. Hitchcock-DeGregori, Tropomyosin: Function follows structure. *Adv. Exp. Med. Biol.* **644**, 60–72 (2008).
4. A. C. Murray, C. M. Kay, Hydrodynamic and optical properties of troponin A. Demonstration of a conformational change upon binding calcium ion. *Biochemistry* **11**, 2622–2627 (1972).
5. S. Ebashi, T. Wakabayashi, F. Ebashi, Troponin and its components. *J. Biochem.* **69**, 441–445 (1971).
6. J. F. Head, S. V. Perry, The interaction of the calcium-binding protein (troponin C) with bivalent cations and the inhibitory protein (troponin I). *Biochem. J.* **137**, 145–154 (1974).
7. H. E. Huxley, Structural changes in the actin- and myosin-containing filaments during contraction. *Cold Spring Harb. Symp. Quant. Biol.* **37**, 361–376 (1972).
8. D. A. D. Parry, J. M. Squire, Structural role of tropomyosin in muscle regulation: Analysis of the x-ray diffraction patterns from relaxed and contracting muscles. *J. Mol. Biol.* **75**, 33–55 (1973).
9. W. Lehman, P. Vibert, P. Uman, R. Craig, Steric-blocking by tropomyosin visualized in relaxed vertebrate muscle thin filaments. *J. Mol. Biol.* **251**, 191–196 (1995).
10. P. Vibert, R. Craig, W. Lehman, Steric-model for activation of muscle thin filaments. *J. Mol. Biol.* **266**, 8–14 (1997).
11. D. F. McKillop, M. A. Geeves, Regulation of the interaction between actin and myosin subfragment 1: Evidence for three states of the thin filament. *Biophys. J.* **65**, 693–701 (1993).
12. J. H. Brown, C. Cohen, Regulation of muscle contraction by tropomyosin and troponin: How structure illuminates function. *Adv. Protein Chem.* **71**, 121–159 (2005).
13. M. V. Vinogradova *et al*., Ca^{2+}-regulated structural changes in troponin. *Proc. Natl. Acad. Sci. U.S.A.* **102**, 5038–5043 (2005).
14. M. A. Geeves, S. S. Lehrer, Cooperativity in the Ca^{2+} regulation of muscle contraction. *Results Probl. Cell Differ.* **36**, 111–132 (2002).
15. S. M. Mijailovich *et al*., Three-dimensional stochastic model of actin-myosin binding in the sarcomere lattice. *J. Gen. Physiol.* **148**, 459–488 (2016).
16. H. E. Huxley, A. Stewart, H. Sosa, T. Irving, X-ray diffraction measurements of the extensibility of actin and myosin filaments in contracting muscle. *Biophys. J.* **67**, 2411–2421 (1994).
17. D. A. Smith, M. A. Geeves, Cooperative regulation of myosin-actin interactions by a continuous flexible chain II: Actin-tropomyosin-troponin and regulation by calcium. *Biophys. J.* **84**, 3168–3180 (2003).
18. Y. Sugimoto *et al*., Structural changes of the regulatory proteins bound to the thin filaments in skeletal muscle contraction by X-ray fiber diffraction. *Biochem. Biophys. Res. Commun.* **369**, 100–108 (2008).
19. N. A. Koubassova, S. Y. Bershitsky, M. A. Ferenczi, A. K. Tsaturyan, Direct modeling of X-ray diffraction pattern from contracting skeletal muscle. *Biophys. J.* **95**, 2880–2894 (2008).
20. X. E. Li *et al*., Tropomyosin position on F-actin revealed by EM reconstruction and computational chemistry. *Biophys. J.* **100**, 1005–1013 (2011).
21. W. Lehman, M. Orzechowski, X. E. Li, S. Fischer, S. Raunser, Gestalt-binding of tropomyosin on actin during thin filament activation. *J. Muscle Res. Cell Motil.* **34**, 155–163 (2013).
22. D. M. Paul, J. M. Squire, E. P. Morris, Relaxed and active thin filament structures; a new structural basis for the regulatory mechanism. *J. Struct. Biol.* **197**, 365–371 (2017).
23. A. Narita, T. Yasunaga, T. Ishikawa, K. Mayanagi, T. Wakabayashi, Ca^{2+}-induced switching of troponin and tropomyosin on actin filaments as revealed by electron cryo-microscopy. *J. Mol. Biol.* **308**, 241–261 (2001).
24. J. von der Ecken *et al*., Structure of the F-actin-tropomyosin complex. *Nature* **519**, 114–117 (2015).
25. C. Risi *et al*., Ca^{2+}-induced movement of tropomyosin on native cardiac thin filaments revealed by cryoelectron microscopy. *Proc. Natl. Acad. Sci. U.S.A.* **114**, 6782–6787 (2017).
26. J. M. Squire, D. M. Paul, E. P. Morris, Myosin and actin filaments in muscle: Structures and interactions. *Subcell. Biochem.* **82**, 319–371 (2017).
27. A. Pirani *et al*., Single particle analysis of relaxed and activated muscle thin filaments. *J. Mol. Biol.* **346**, 761–772 (2005).
28. K. X. Ngo, N. Kodera, E. Katayama, T. Ando, T. Q. Uyeda, Cofilin-induced unidirectional cooperative conformational changes in actin filaments revealed by high-speed atomic force microscopy. *eLife* **4**, e04806 (2015).
29. J. Hanson, Evidence from electron microscope studies on actin paracrystals concerning the origin of the cross-striation in the thin filaments of vertebrate skeletal muscle. *Proc. R. Soc. Lond. B Biol. Sci.* **183**, 39–58 (1973).
30. E. H. Egelman, N. Francis, D. J. DeRosier, F-actin is a helix with a random variable twist. *Nature* **298**, 131–135 (1982).
31. E. J. O'Brien, M. J. Dickens, "Actin and thin filaments" in *Electron Microscopy of Proteins*, J. R. Harris, Ed. (Academic Press, London, 1983), pp. 1–95.
32. P. Vibert, R. Craig, Three-dimensional reconstruction of thin filaments decorated with a Ca^{2+}-regulated myosin. *J. Mol. Biol.* **157**, 299–319 (1982).
33. M. Orzechowski, X. E. Li, S. Fischer, W. Lehman, An atomic model of the tropomyosin cable on F-actin. *Biophys. J.* **107**, 694–699 (2014).
34. C. Xu, R. Craig, L. Tobacman, R. Horowitz, W. Lehman, Tropomyosin positions in regulated thin filaments revealed by cryoelectron microscopy. *Biophys. J.* **77**, 985–992 (1999).
35. D. R. Sousa, S. M. Stagg, M. E. Stroupe, Cryo-EM structures of the actin:tropomyosin filament reveal the mechanism for the transition from C- to M-state. *J. Mol. Biol.* **425**, 4544–4555 (2013).
36. T. Ando *et al*., A high-speed atomic force microscope for studying biological macromolecules. *Proc. Natl. Acad. Sci. U.S.A.* **98**, 12468–12472 (2001).
37. N. Kodera, D. Yamamoto, R. Ishikawa, T. Ando, Video imaging of walking myosin V by high-speed atomic force microscopy. *Nature* **468**, 72–76 (2010).
38. D. Yamamoto, N. Nagura, S. Omote, M. Taniguchi, T. Ando, Streptavidin 2D crystal substrates for visualizing biomolecular processes by atomic force microscopy. *Biophys. J.* **97**, 2358–2367 (2009).
39. J. Kozuka, H. Yokota, Y. Arai, Y. Ishii, T. Yanagida, Dynamic polymorphism of single actin molecules in the actin filament. *Nat. Chem. Biol.* **2**, 83–86 (2006).
40. A. Narita *et al*., Direct observation of the actin filament by tip-scan atomic force microscopy. *Microscopy (Oxf.)* **65**, 370–377 (2016).
41. T. L. Hill, E. Eisenberg, L. Greene, Theoretical model for the cooperative equilibrium binding of myosin subfragment 1 to the actin-troponin-tropomyosin complex. *Proc. Natl. Acad. Sci. U.S.A.* **77**, 3186–3190 (1980).
42. R. Desai, M. A. Geeves, N. M. Kad, Using fluorescent myosin to directly visualize cooperative activation of thin filaments. *J. Biol. Chem.* **290**, 1915–1925 (2015).
43. H. Isambert *et al*., Flexibility of actin filaments derived from thermal fluctuations. Effect of bound nucleotide, phalloidin, and muscle regulatory proteins. *J. Biol. Chem.* **270**, 11437–11444 (1995).
44. E. H. Egelman, A. Orlova, Allostery, cooperativity, and different structural states in F-actin. *J. Struct. Biol.* **115**, 159–162 (1995).
45. M. J. Greenberg, C. L. Wang, W. Lehman, J. R. Moore, Modulation of actin mechanics by caldesmon and tropomyosin. *Cell Motil. Cytoskeleton* **65**, 156–164 (2008).
46. E. Bengtsson *et al*., Myosin-induced gliding patterns at varied [MgATP] unveil a dynamic actin filament. *Biophys. J.* **111**, 1465–1477 (2016).
47. A. Houdusse, H. L. Sweeney, How myosin generates force on actin filaments. *Trends Biochem. Sci.* **41**, 989–997 (2016).
48. E. Behrmann *et al*., Structure of the rigor actin-tropomyosin-myosin complex. *Cell* **150**, 327–338 (2012).
49. R. Craig, W. Lehman, The ultrastructural basis of actin filament regulation. *Results Probl. Cell Differ.* **36**, 149–169 (2002).
50. J. H. Snook, J. Li, B. P. Helmke, W. H. Guilford, Peroxynitrite inhibits myofibrillar protein function in an in vitro assay of motility. *Free Radic. Biol. Med.* **44**, 14–23 (2008).
51. M. Persson, E. Bengtsson, L. ten Siethoff, A. Månsson, Nonlinear cross-bridge elasticity and post-power-stroke events in fast skeletal muscle actomyosin. *Biophys. J.* **105**, 1871–1881 (2013).
52. A. Kalganov *et al*., Forces measured with micro-fabricated cantilevers during actomyosin interactions produced by filaments containing different myosin isoforms and loop 1 structures. *Biochim. Biophys. Acta* **1830**, 2710–2719 (2013).
53. Y. S. Cheng, O. S. Matusovskiy, D. E. Rassier, Cleavage of loops 1 and 2 in skeletal muscle heavy meromyosin (HMM) leads to a decreased function. *Arch. Biochem. Biophys.* **661**, 168–177 (2019).
54. T. Uchihashi, N. Kodera, T. Ando, Guide to video recording of structure dynamics and dynamic processes of proteins by high-speed atomic force microscopy. *Nat. Protoc.* **7**, 1193–1206 (2012).
55. T. Ando *et al*., "High-speed AFM for observing dynamic processes in liquid" in *Atomic Force Microscopy in Liquid: Biological Applications*, A. M. Baró, R. G. Reifenberger, Eds. (Wiley, 2012), pp. 189–209.